

Article

Application of a Pre-Trained CNN Model for Fault Interpretation in the Structurally Complex Browse Basin, Australia

Md Mahmudul Islam ^{*}, Ismailalwali Babikir, Mohamed Elsaadany, Sami Elkurdy, Numair A. Siddiqui and Oluwaseun Daniel Akinyemi

Centre for Subsurface Imaging, Department of Geosciences, Universiti Teknologi PETRONAS, Bandar Seri Iskandar, Tronoh 32610, Malaysia; ismailalwal_19001505@utp.edu.my (I.B.); mohamed.elsaadany@utp.edu.my (M.E.); selkurdy@gmail.com (S.E.); numair.siddiqui@utp.edu.my (N.A.S.); oluwaseun_22000009@utp.edu.my (O.D.A.)

* Correspondence: md_22005140@utp.edu.my

Abstract: Fault detection is an important step in subsurface interpretation and reservoir characterization from 3D seismic images. Due to the numerous and complex fault structures in seismic images, manual seismic interpretation is time-consuming and requires intensive work. We applied a pre-trained CNN model to predict faults from the 3D seismic volume of the Poseidon field in the Browse Basin, Australia. This field is highly structured with complex normal faulting throughout the targeted Plover Formations. Our motivation for this work is to compare machine-learning-based fault prediction to user-interpreted fault identification supported by seismic variance attributes. We found reasonably satisfactory results using CNN with an improved fault probability volume that outperforms variance technology. Therefore, we propose that this workflow could reduce time and be able to predict faults quite accurately in most structurally complex areas.

Keywords: fault detection; reservoir characterization; seismic images; convolutional neural network; variance attribute



Citation: Islam, M.M.; Babikir, I.; Elsaadany, M.; Elkurdy, S.; Siddiqui, N.A.; Akinyemi, O.D. Application of a Pre-Trained CNN Model for Fault Interpretation in the Structurally Complex Browse Basin, Australia. *Appl. Sci.* **2023**, *13*, 11300. <https://doi.org/10.3390/app132011300>

Academic Editors: José A. Peláez, Roberto Scarpa, Sanyi Yuan and Peidong Shi

Received: 11 July 2023

Revised: 4 September 2023

Accepted: 12 September 2023

Published: 14 October 2023



Copyright: © 2023 by the authors. Licensee MDPI, Basel, Switzerland. This article is an open access article distributed under the terms and conditions of the Creative Commons Attribution (CC BY) license (<https://creativecommons.org/licenses/by/4.0/>).

1. Introduction

The interpretation of seismic faults is an essential stage for both the exploration and development of reservoir characterization [1]. Because manual fault interpretation is time-consuming, implementing computer-aided techniques is tested in this study. Several approaches to extract faults from seismic data have been proposed over the past decades [2,3]. Seismic discontinuity attributes were developed to visually detect faults and fractures [4]. To understand stratigraphic and structural geological features in seismic data volumes, seismic edge-detection algorithms have been very popular and extensively applied in the industry [5–8]. Many researchers have utilized different attributes for detecting faults such as the curvature [2,9], variance [10–12], semblance [4,13], coherency [14–17], eigenstructure [18,19], fault likelihood [19,20], similarity [8,21,22], entropy [23], flexure [3,24,25], gradient magnitude [26], chaos [26,27], and derivatives [3,18,28,29]. In earlier research, Rijks et al. (1991) presented how the azimuth and dip magnitude may reveal very tiny faults with movement substantially lower than that of a seismic wavelet [30]. Reflective curvature analysis has also been used to discover faults in migrating geological data using reflector geometry, as well as to map and predict fracture orientations and distribution via flexure and edge detection [24,31]. However, misclassification is sometimes observed when attribute-based techniques fail to distinguish the faults from the neighboring unfaulted features due to the extraction of limited numbers of attributes in seismic data [32,33].

On the other hand, many researchers have tried to incorporate the advanced techniques of machine learning (ML) and deep learning (DL) in detecting faults in seismic images such as multi-layer perceptron (MLP), convolutional neural network (CNN), principal component analysis (PCA), deep convolutional neural network (DCNN), as well as

CNN pre-trained on synthetic data [2,34,35]. However, the accuracy of these workflows when compared to multi-attribute-based classification is mostly reliant on the expertise of the interpreter in selecting a set of attributes to distinguish complex geologic features and faults. Furthermore, the attribute selection technique must be repeated from one seismic dataset to the next [36]. Many techniques and procedures for better fault detection have been proposed because of the severe limitations of the conventional fault interpretation, and some have been implemented successfully. These approaches include those that solely focus on enhancing the 3D representation of seismic data using attributes, meta-attributes, filters, soft computing, and machine-learning algorithms. Machine-learning techniques are often used in fields where conventional approaches are otherwise time-consuming due to the allegedly achieved results in these fields [4]. Filtering the data to eliminate the negative effects of noise may aid in smoothing reflectors and sharpening for fault interpretation. Several noise attenuation techniques have proved useful in this area, whether utilized during the acquisition stage or subsequently [1].

Over the years, there have been tremendous advancements in the exploration of seismic faults in the context of reservoir characterization, but there is still an obvious research deficit. Prior research included attribute-based methods and even machine-learning strategies in an effort to improve fault detection methods. These attempts, which frequently rely primarily on manual attribute selection, have been hampered by the difficulty of consistently differentiating complex geological structures and faults across several seismic datasets [32,36]. The critical importance of our study region, the Poseidon field in the Browse Basin, Australia, is highlighted by this knowledge gap. The distinctive geological features of the Poseidon field, characterized by complex normal faulting throughout the target Plover Formations, present a unique mix of difficulties and opportunities for seismic fault investigation. In this paper, we compared the traditional manual fault interpretation with a pre-trained CNN model on 3D seismic data from the Poseidon field of the Browse Basin, Australia. The motivation of this work is to demonstrate that the pre-trained CNN-based fault prediction is more efficient and time-saving when compared to variance-guided manually interpreted faults.

This paper's subsequent sections are organized as follows: Section 2 describes the geological setting of the chosen area. Section 3 describes the research methodology, including the variance-guided manual fault picking and pre-trained CNN-driven fault prediction. Section 4 presents an in-depth analysis and comparison of the findings of CNN with variance. Section 5 provides a discussion of the feasibility of the pre-trained CNN model. Finally, Section 6 concludes with a concise summary of the study's contributions and a discussion of the future prospects of the pre-trained CNN model.

2. Geological Setting

The Australian North-West Shelf (NWS) Browse Basin is a passive continental margin that stretches between the latitudes of 21° and 13° S from the SW to the NE. The Browse Basin is located in the southern edge of the Timor Sea, between the Scott Plateau to the west, the offshore Kimberley Block to the north, and the Scott Plateau to the east. It covers an area of over 140,000 km², and its sedimentary depth exceeds 15 km (Figure 1). On the NWS, it is one of several lengthy sedimentary basins. The area evolved via six geological periods, from early Carboniferous to Late Jurassic inversion to late Cretaceous inversion. Thermal subsidence occurred during the Permian and Triassic ages. The central Browse Basin is a margin-parallel half-graben system that structurally dips towards the continent [37]. The break-up of Greater India from Western Australia resulted in either a single phase or two phases of rifting, which led to the development of the NWS [38]. A thick succession of passive edge sediment was deposited in the Browse Basin after tectonic activity in the Aptian had halted, burying the old structural relief [39]. Several petroleum systems have been determined, implying that at least three major petroleum systems exist.

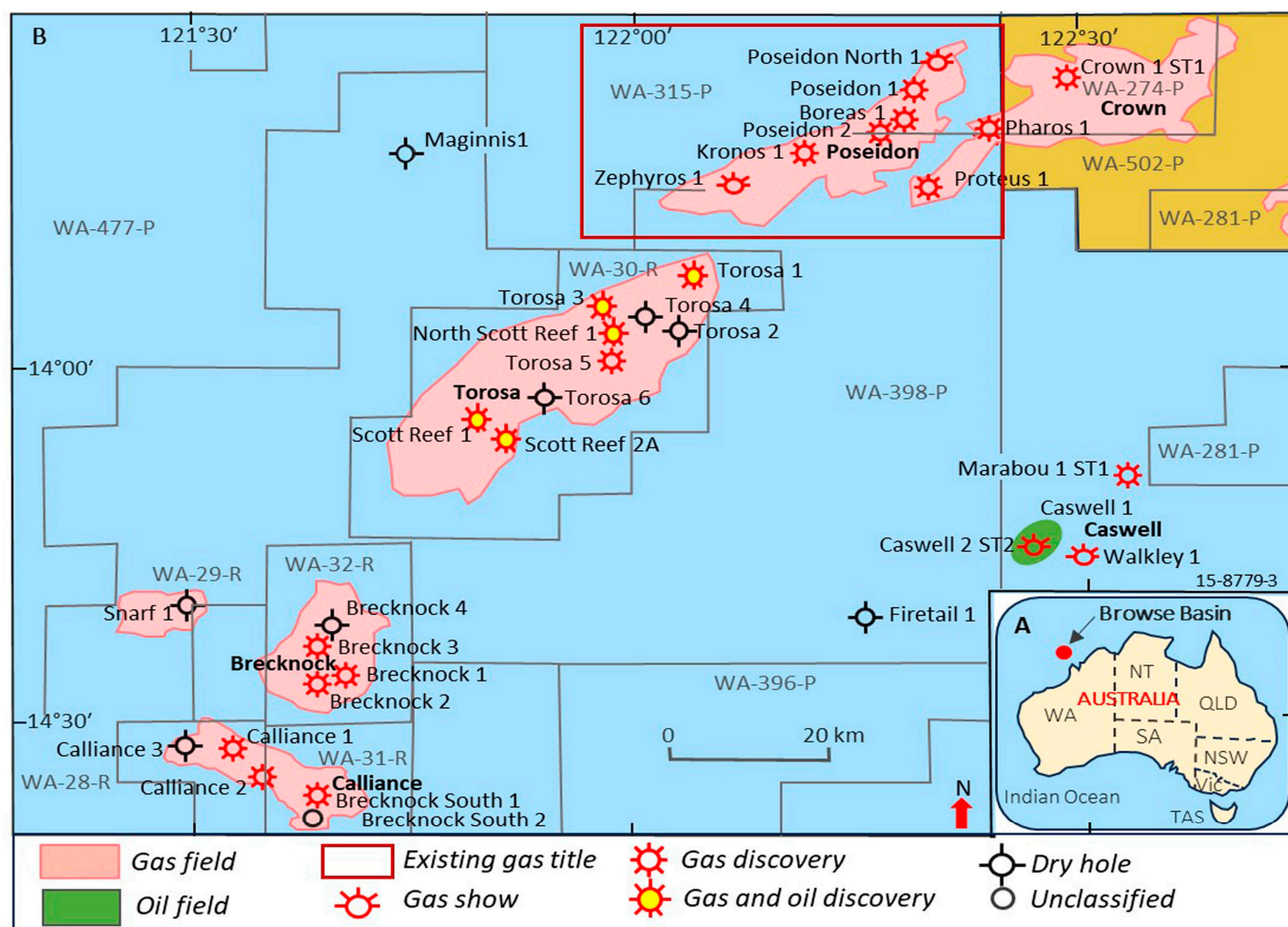


Figure 1. (A) Location of Browse Basin, Australia, on the world map. (B) Location of different sub-basins (Poseidon, Crown, Torosa, Brecknock, Calliance, and Caswell) where the rectangular red block represents the Poseidon field that is our study area (modified after [40]). Reprinted with permission from Springer Nature.

The primary structural patterns in the Browse Basin were likely produced by the final stage of rifting that occurred in the Middle Jurassic–Early Cretaceous (Figure 2). The Plover Formation is made up of a series of stacked fluvio-deltaic and shallow marine sands, shales, and silts, as well as trace amounts of carbonate and volcanic materials during active faulting of the Jurassic extension [40]. As a result, the thickness and lateral continuity of this formation range approximately 200–450 m thick; sandstones are extensively variable throughout the basin. A regional unconformity is marked at the base of the Plover Formation whereas the top of Plover is defined as Late Callovian age unconformity. A significant volcanic province is present in the Browse Basin throughout the Early to Late Jurassic [41]. Most traps in the area are structural; however, there is potential for chronological traps on the margins of existing structures and alluvial/submarine fans dumped on the hanging wall of significant horsts. The rifting is related to volcanic activity, which might deteriorate reservoir quality and absorb habitation space, inhibiting sandstone deposition [40]. The research area's source rocks were deposited in the broad fluvial-deltaic channels that spanned most of the basin. Prodelta shales, coaly shales, and shallow coals harboring abundant marine organic materials are examples. Applying well data, the Near Top Plover Formation has been examined and is interpreted as an upward increase in acoustic impedance. The structure of the rocks above and below this barrier is thought to be varied, with the possibility of sand on shale, shale on shale, and shale on sand interfaces. As a result, the seismic marker at the Near Top Plover Formation varies spatially [42]. The Near Top Plover

horizon is distinguished by underlying complex faulting. Normal faults resulted in a series of fault ridges and grabens. This makes detecting and delineating the Plover Formation’s gas saturated reservoir extremely challenging for the Browse Basin [43].

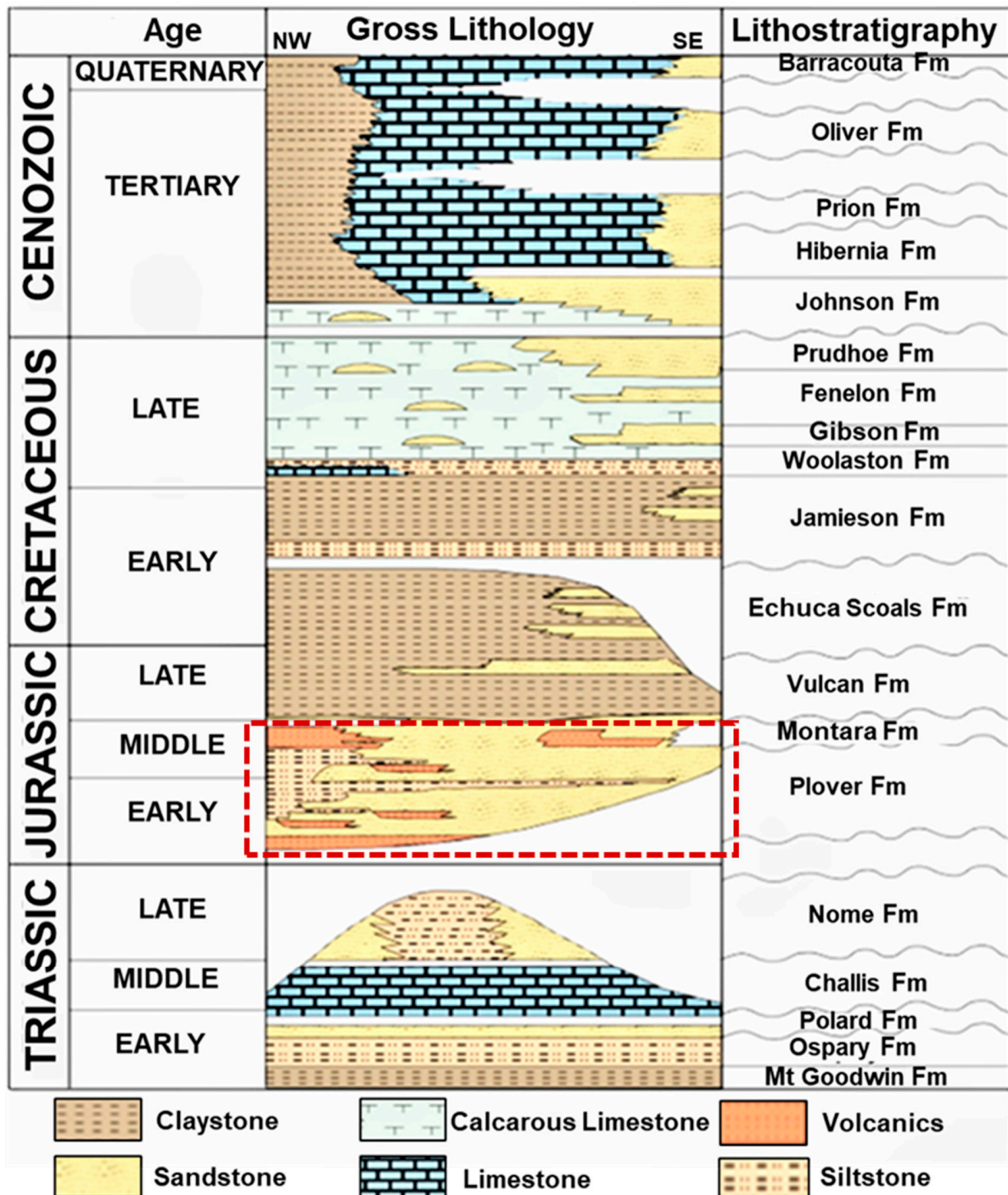


Figure 2. Generalized lithostratigraphic column of Browse Basin, Australia. The rectangular red-dash block marks the focus area of this study (modified after [40]). Reprinted with permission from Springer Nature.

3. Materials and Methods

3.1. Dataset

The available data for this study were provided by the Society of Exploration Geophysicists. The dataset includes 3D seismic data in SEG-Y format that have 1600 and

1800 inlines and crosslines with a sample interval of 4 ms and a number of samples per trace of 501. The inline interval is 18.75 m whereas the crossline interval is 12.50 m. Also, the time interval of this seismic cropped volume is from 2000 ms to 4000 ms with normal polarity.

The dataset also includes six wells (Boreas-1, Kronos-1, Pharos-1, Poseidon-1, Poseidon-2, and Proteus-1) with petrophysical logs in ASCII las format, and formation markers, deviation survey, and five velocity check-shots in ASCII format. These wells were used to conduct a structural interpretation of a cropped Poseidon field of the Browse Basin. Five types of wireline logs (gamma ray, resistivity, density, neutron, and sonic logs) are available with this dataset.

3.2. Methodology

The study followed the workflow shown in Figure 3. The workflow commenced with well correlation and synthetic seismogram generation to establish a robust seismic-to-well tie. Subsequently, horizons and faults were manually picked throughout the entire 3D volume. Two horizons, namely the Top and Base of the Plover Formation, representing the interval of interest within the highly faulted synrift deposits, were interpreted. Additionally, faults that intersected with the interval of interest were picked. The variance attribute, a widely used discontinuity attribute for highlighting faults, fractures, and stratigraphic boundaries, was generated in Petrel Software (version 2020) with an IL 3 by XL 3 and 15 samples of vertical smoothing with no dip correction and displayed along the top of the Plover Formation to provide constraints and assist in fault interpretation. A 3D Gaussian filter was applied prior to the computation of the variance to reduce random noise. A time structure map was then constructed using the manually interpreted faults and horizons to illustrate the faulting system and structural configuration of the rifted interval. This part of the study is predominantly interpreter-driven, relying on knowledge and experience as it has a lot of uncertainties and is time-consuming.

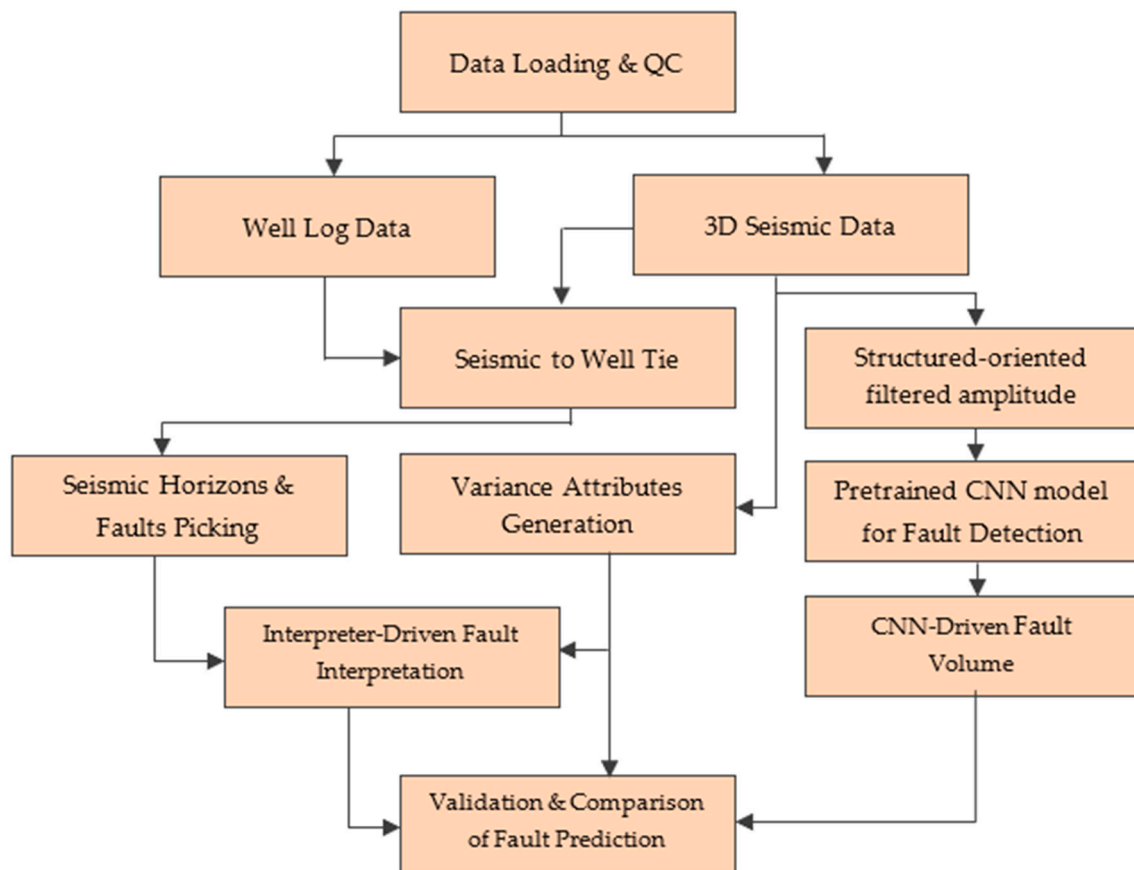


Figure 3. The workflow used in this study.

The second part of the study was entirely data-driven, involving the application of pre-trained deep-learning models to filtered seismic amplitude data for the automatic prediction of faults within the entire seismic volume. The final step in the workflow was to validate and compare the outputs of both the traditional interpreter-guided and the CNN-driven approaches.

Deep-Learning-Based Fault Prediction

A pre-trained CNN model was trained by Geophysical Insight in their Paradise software on the SEAM (SEG Advanced Modelling) model which is a large synthetic dataset. Numerous sub-volumes were extracted from the impedance model and faults were inserted. These were used as the realistic synthetic training dataset. The CNN model attempts to identify locally reflected seismic patterns ignoring numerous artefacts and noise present in the segy 3D in the process. A general CNN workflow used for automatic fault prediction is shown in Figure 4. This workflow normally consists of a simple 1-layer CNN network followed by one fully connected layer for fault classification. Seismic input images are 32 by 32 pixels. The convolution masks (kernel) are 9×9 pixels in size. In the convolutional layer, 16 features are produced. The dimensions of the output features after convolution are reduced using 2×2 maximum pooling, which also controls overfitting. The SoftMax cross entropy is performed to determine the probability error between the classification and the true labels, and the fully connected layer contains 1024 neurons. The model is a binary classification identifying the presence/absence of a fault.

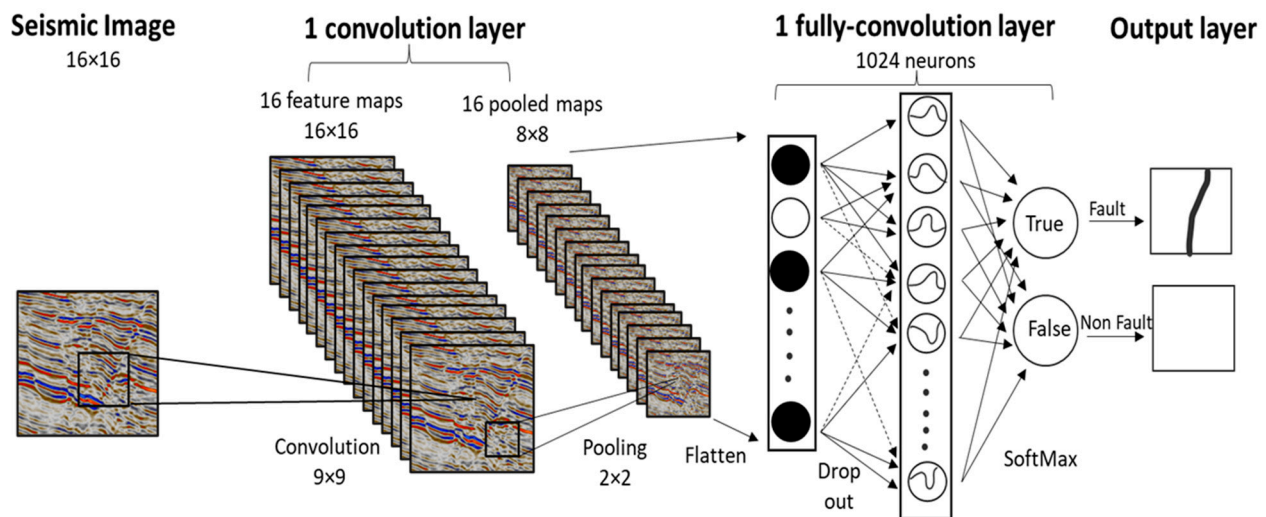


Figure 4. The general CNN workflow used for fault prediction (modified after [44]). Reprinted with permission from the Society of Exploration Geophysicists.

In this study, pre-trained CNN models, available in the Paradise software, were applied to automatically predict faults. The workflow in Paradise involves applying structurally oriented filtering (named SOF3D) to sharpen the discontinuities of the seismic amplitude volume before applying the CNN models. It is a useful strategy for eliminating incoherent noise and enhancing event continuity without smoothing over dipping planes [45,46]. Three different architecture models operated on the data, known as aggressive, conservative, and mixed-angle engine. Both conservative and aggressive models were trained on synthetic faults with high angles, while the mixed-angle model was trained on faults with varying angles. The conservative CNN model produced fewer false positives and mostly identified continuous faults, whereas the aggressive model revealed more discontinuities in seismic amplitude data with shorter and less continuous fault identification in 3D. The mixed-angle model generally works well on data of varying angle faults. In the current study, we found that the result of the mixed-angle model is geologically meaningful.

4. Results

Three-dimensional seismic imaging does not usually offer sharp imaging of faults and is sometimes ambiguous regarding fault geometry and continuity. In Figure 5C, we present the results of our interpreted horizons alongside manually picked faults to delineate geological features on inline 2940. Figure 5D reveals the outcome of our CNN model on the same inline which displayed remarkable resemblances to the manually picked faults.

Fault polygons were created manually after picking the horizon of the top and base of the Lower Plover Formation (LPF) and a Two-Way Time (TWT) structure map was generated from the picked horizons (Figure 6). From the structure map it is observed that most of the faults are trending in a NW to SE direction. The reservoir zone lies between 3250 ms and 3500 ms on average, but the northern block is down-faulted to about 3700 ms.

A deep-learning (DL) automatic fault detection pre-trained CNN algorithm was also applied to same 3D. The DL-identified faults are compared to the conventionally picked faults and variance lineaments. Deep-Learning CNN fault identification is shown in Figure 7B at a time slice of 3464 ms.

There were three fault interpretation cases observed and investigated on both variance and CNN automatic fault detection.

Case 1 represents faults that are clearly visible in both variance and CNN, Case 2 represents faults that are clearly visible in CNN but not in variance, and lastly Case 3 represents faults that are visible in variance but not detected or identified on CNN. In the following sections, a few examples from each case are shown.

To facilitate the comparisons, a time slice of 3464 ms from both variance (Figure 7A) and CNN cubes (Figure 7B) was selected due to its proximity to the horizon of the Top Plover Formation. A few 3D arbitrary seismic sections crossing some faults were selected to demonstrate the clarity of event terminations for fault detection.

Case 1. *Faults clearly visible on both variance and CNN cubes.*

As expected, almost all faults fell in this category. A few examples were selected to be presented. In Figure 8, clear continuous N-S trending fault (F) is seen on CNN (E) whereas it is seen as two disconnected segments on variance. In the vertical sections the faults show clearly. Spatial fault continuity is not clear on the variance slice as compared to that of the CNN. Another 3D arbitrary seismic section that crosses the gap between the two variance fault segments clearly shows the event terminations.

In Figure 9, a different area showing two faults detected on both variance and CNN automatic fault detection. On the vertical seismic section (a'-b'), F₁ fault is clearly seen whereas F₂ fault is not. It is observed that a fault detected on the CNN time slice (F₂) is not observed on the vertical seismic section. On the other hand, that same fault (F₂) is also not observed on the variance slice. This raises a question as to the validity of the detected lineament on the CNN slice.

Faults detected on both variance cube and CNN model are shown in Figure 10. The lateral extent of the fault on the CNN slice is quite shorter than that seen on the variance slice, even though the fault is quite distinct on the vertical seismic section.

Case 2. *Faults clearly visible on CNN but not on variance cubes.*

This case demonstrates the value of CNN-identified lineaments that are not detected by the variance. Figure 11 represents an example of a fault that is detected on both variance and CNN, but does not extend far enough on the variance, even though it is quite clear on the vertical seismic section (a'-b').

Case 3. *Faults clearly visible on variance but not on CNN cubes.*

In Figure 12, the fault under consideration is seen on the variance cube but does not exist on the CNN slice. The vertical section supports the existence of the fault, which was missed on the CNN slice.

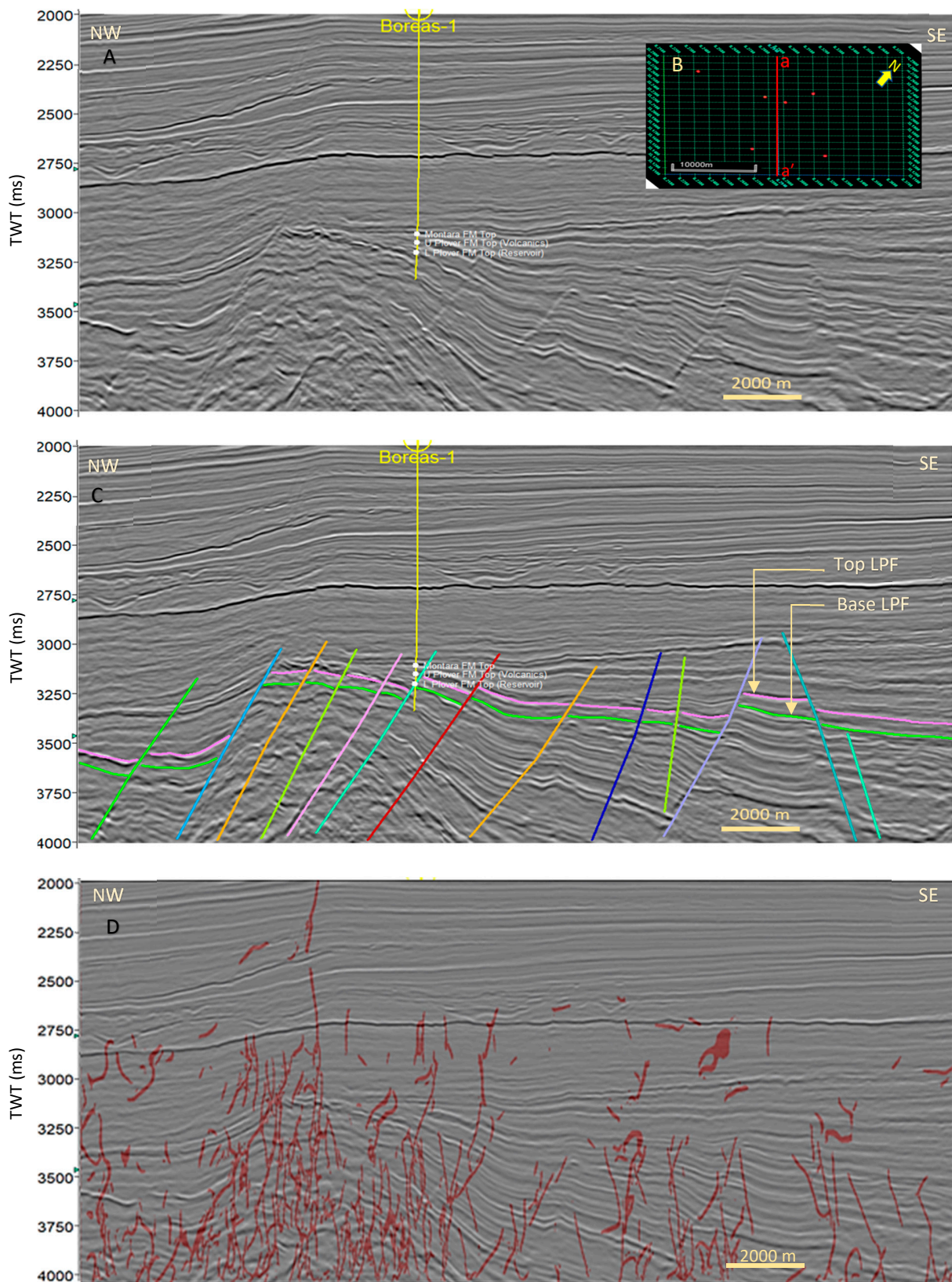


Figure 5. (A) Uninterpreted seismic inline 2940. (B) Base map showing location of displayed inline a-a' and red circles represent well locations. (C) Interpreter-driven manual horizons and fault picking shown with different colored lines. (D) CNN-driven fault prediction on the same inline 2940.

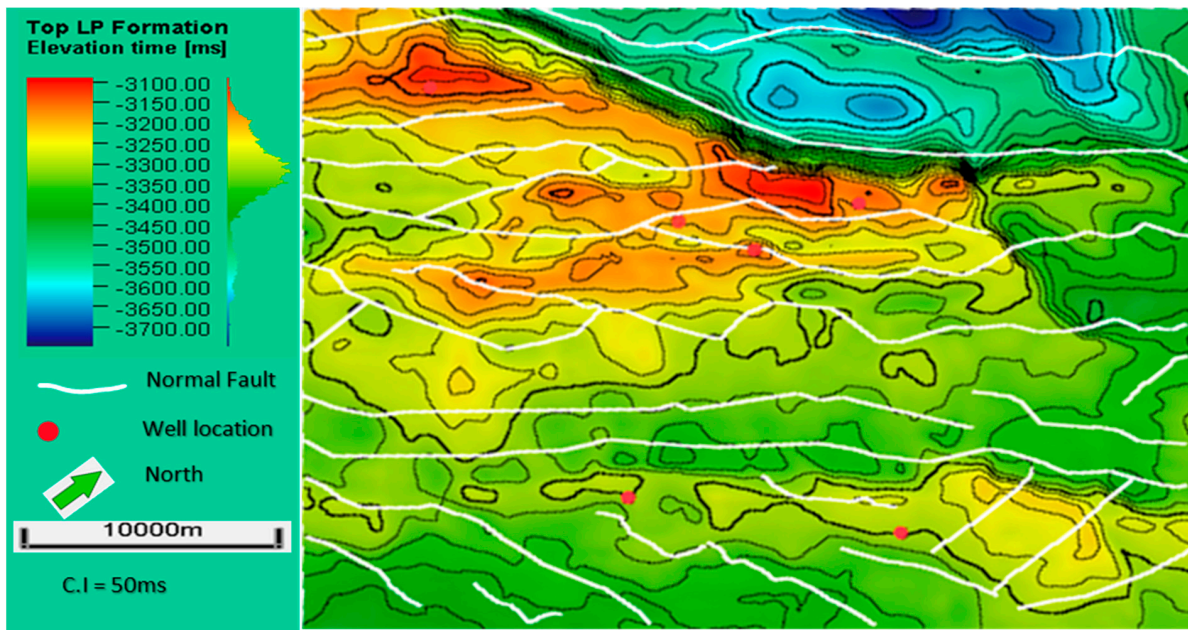


Figure 6. Two-way time structure map of Top Lower Plover Formation.

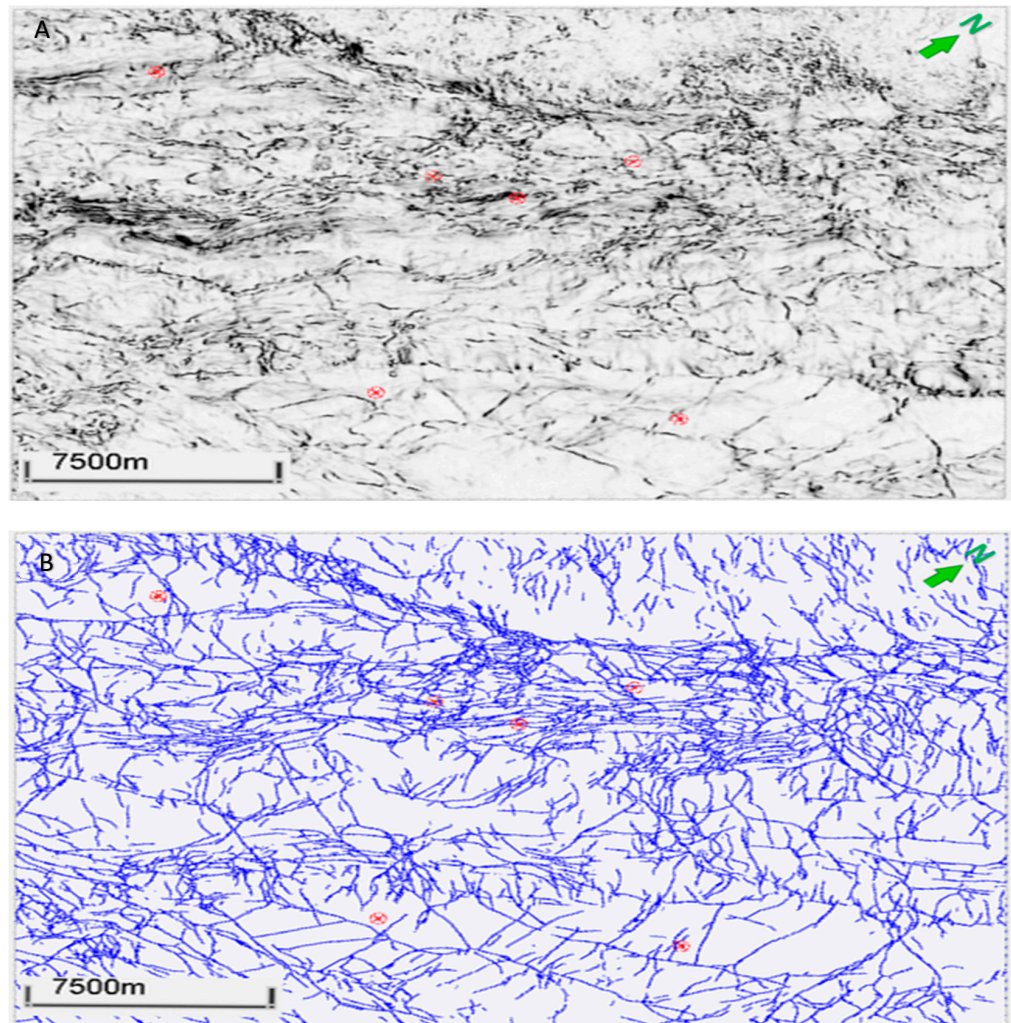


Figure 7. Cont.

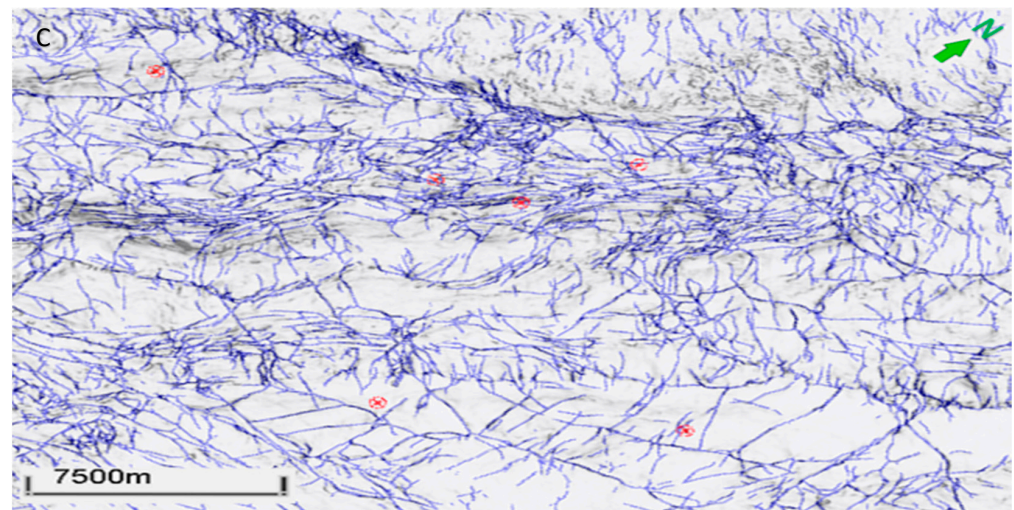


Figure 7. (A) Fault detection using variance attributes at 3464 ms. (B) Fault prediction using CNN at a time slice of 3464 ms. (C) Validation of the predicted faults by overlaying variance and CNN slice at 3464 ms.

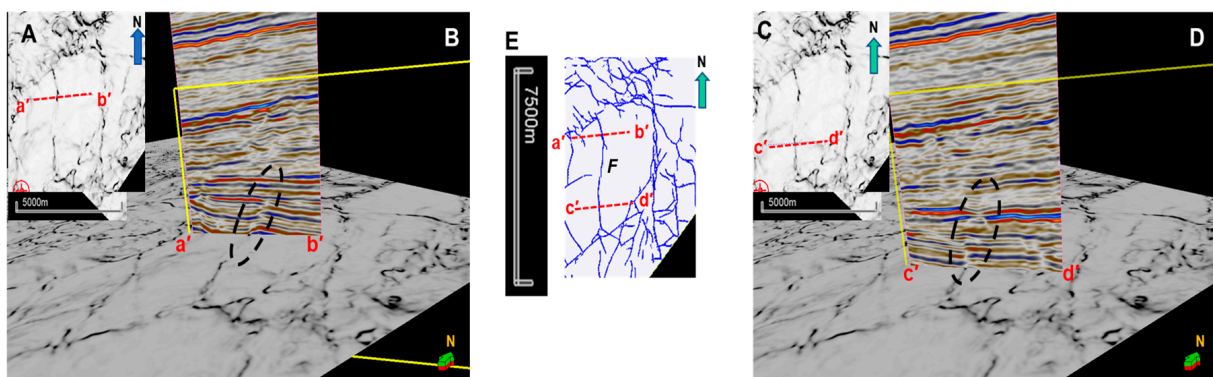


Figure 8. (A,B) Map view of 3464 ms TWT variance seismic attribute slice and DL showing the location of the a'-b' and c'-d' 3D arbitrary seismic sections. (C) Three-dimensional view of 3464 ms TWT variance seismic attribute slice with a'-b' 3D arbitrary seismic section. (D) Three-dimensional view of 3464 ms TWT variance seismic attribute slice with c'-d' 3D arbitrary seismic section. (E) CNN automatic fault detection 3464 ms TWT map view showing the c'-d' 3D arbitrary seismic section locations. The black dashed ellipsoid on Figure 9B,D shows a clear fault in the 3D arbitrary vertical seismic section.

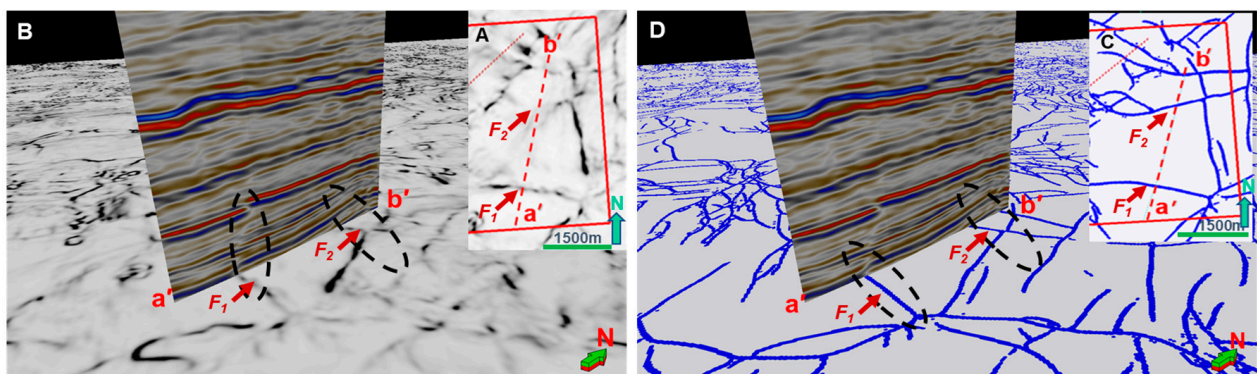


Figure 9. Cont.

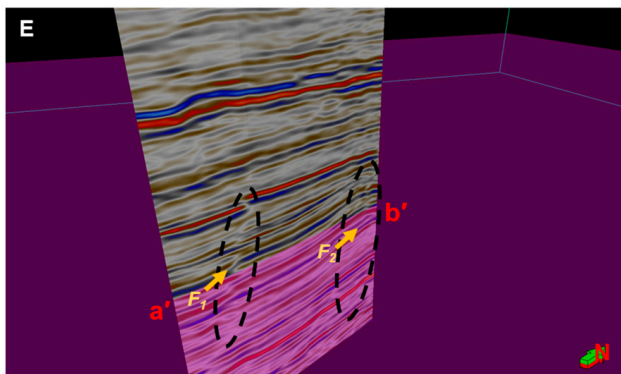


Figure 9. (A) Map view of 3464 ms TWT variance seismic attribute slice showing the location of the a'-b' 3D arbitrary seismic section. (B) Three-dimensional view of 3464 ms TWT variance seismic attribute slice with a'-b' 3D arbitrary seismic section. (C) Map view of 3464 ms CNN TWT slice showing the location of the a'-b' 3D arbitrary seismic section. (D) Three-dimensional view of 3464 ms TWT CNN slice with a'-b' 3D arbitrary seismic section. (E) Three-dimensional view of transparent dummy slice at TWT (3464 ms) with a'-b' 3D arbitrary seismic section. The black dashed ellipsoid shows a clear fault in the 3D arbitrary vertical seismic section, variance, and CNN automatic fault detection (F₁), and a fault only visible on the CNN time slice (F₂).

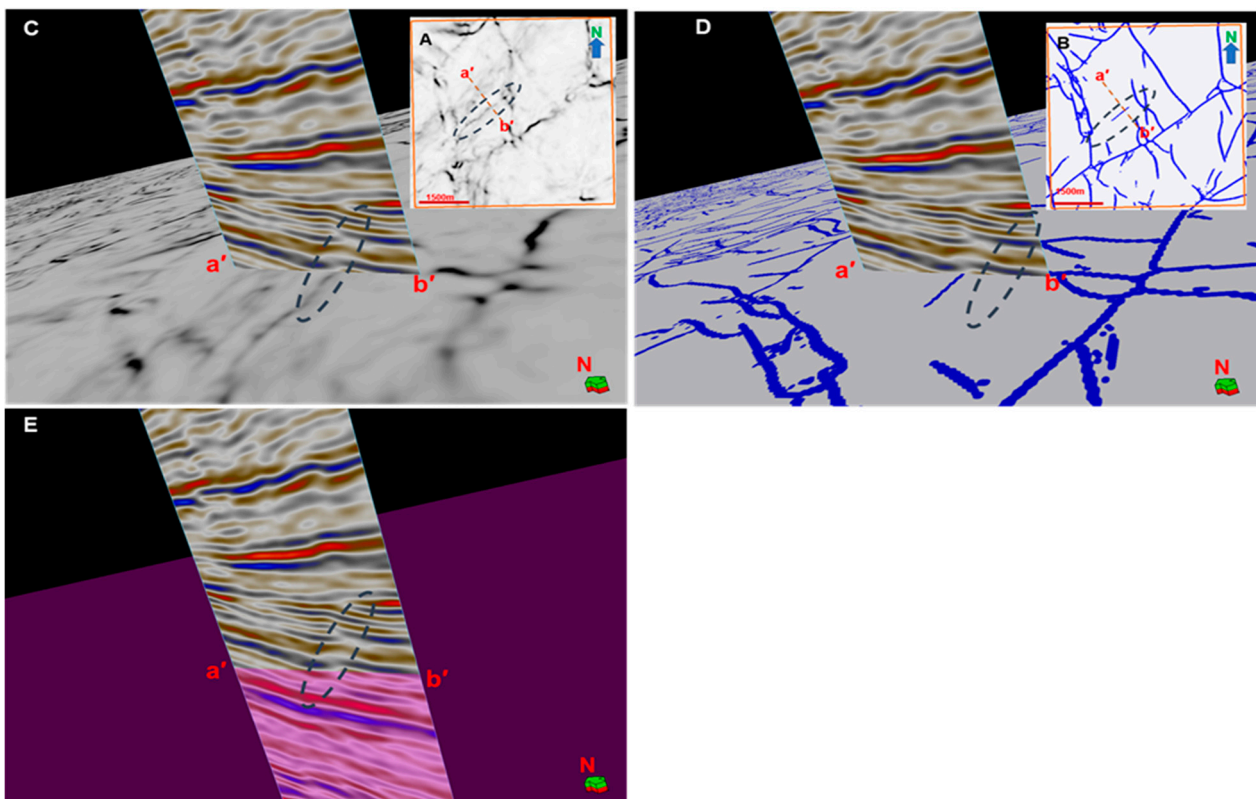


Figure 10. (A,B) Map view of 3464 ms variance seismic attribute and CNN automatic fault detection TWT slice showing the location of the a'-b' 3D arbitrary seismic section. (C) Three-dimensional view of 3464 ms variance seismic attribute TWT slice. (D) Three-dimensional view of 3464 ms CNN automatic fault detection TWT slice. (E) Transparent dummy slice at TWT (3464 ms). The black dashed ellipsoid clearly shows the fault under investigation.

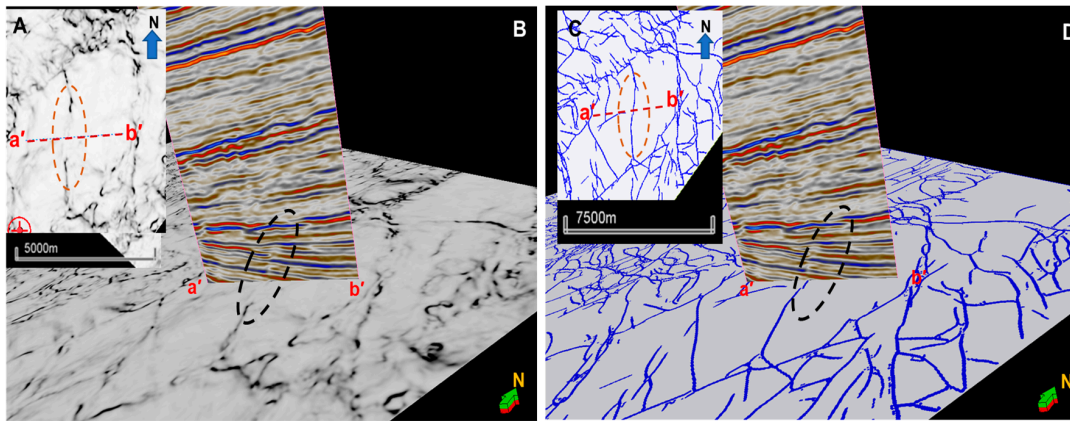


Figure 11. (A,C) Map view of 3464 ms variance seismic attribute and CNN automatic fault detection TWT slice showing the location of the a'-b' 3D arbitrary seismic section. (B) Three-dimensional view of 3464 ms variance seismic attribute TWT slice. (D) Three-dimensional view of 3464 ms CNN automatic fault detection TWT slice. The black ellipsoid shows clear faults on the 3D arbitrary seismic section and CNN automatic fault detection time slice while they do not show on the variance time slice.

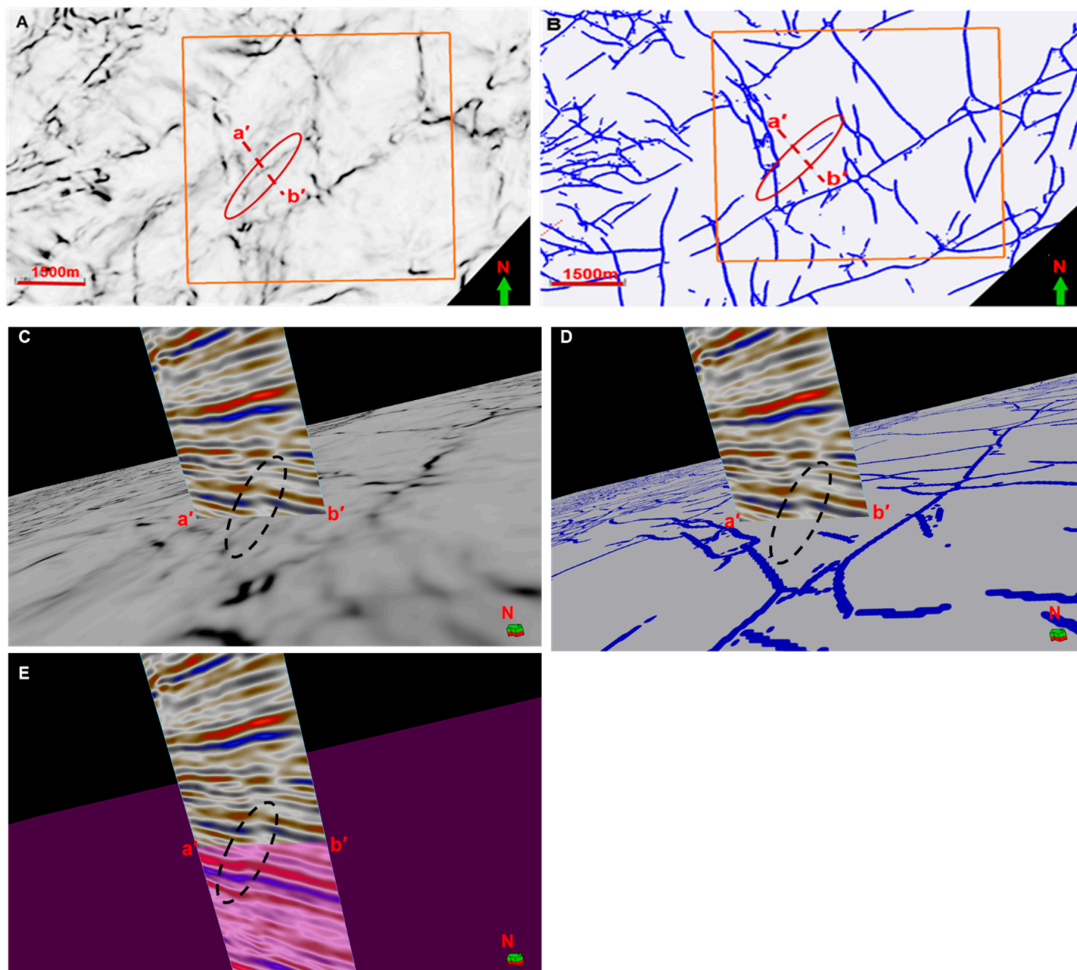


Figure 12. (A,B) Map view of 3464 ms variance seismic attribute and CNN automatic fault detection TWT slice showing the location of the a'-b' 3D arbitrary seismic section. (C) Three-dimensional view of 3464 ms variance seismic attribute TWT slice. (D) Three-dimensional view of 3464 ms CNN automatic fault detection TWT slice. (E) Transparent dummy slice at TWT (3464 ms). The black ellipsoid shows a clear fault on variance and the vertical 3D seismic arbitrary a-b section whereas it is not seen on CNN automatic fault detection.

5. Discussion

Most of the faults identified by variance and/or CNN can be interpreted using conventional and manual picking but these are more time-consuming and demand high interpretation skills and structural geology domain experience. The CNN-based approach has significant advantages over traditional fault detection techniques. With the traditional approach, we need to apply fault enhancement, e.g., variance, to optimize fault detection. Even though the CNN model can efficiently pick almost all lineaments, it is still dependent on the broad coverage of the training dataset. A pre-trained CNN model of Paradise software was trained on synthetic data. Out of the three architectures of this model known as aggressive, conservative, and mixed-angle engine, only the mixed-angle engine results were found to be geologically accurate. In terms of comparison of manually interpreted faults with ML, Figure 5A shows a vertical slice with many major listric normal faults that were manually interpreted (Figure 5C) on seismic inline 2940 to a lesser extent than the CNN results (Figure 5D) on the same inline. The CNN fault results provide cleaner fault anomalies by capturing all subtle faults that are unable to be mapped easily by a human interpreter. Moreover, from the critical analysis of the three cases demonstrated in Figures 8–12, the pre-trained CNN model shows slightly more continuous faults (Figure 7B) than the variance cube shown in Figure 7A. These findings highlight the effectiveness of the pre-trained CNN-based fault prediction in strengthening fault identification in seismic data. In addition, this pre-trained CNN model does not require any manual interpretation of faults and needs approximately three hours (which might vary depending on data size) to provide the fault prediction findings of the seismic volume. This approach was demonstrated in real-world applications of CNN using transfer learning in seismic fault detection. Exploring the feasibility of employing transfer learning, especially fine tuning a pre-trained CNN model with the actual seismic data of the Poseidon field, offers a promising avenue for further improving the fault prediction accuracy in this complex geological setting.

6. Conclusions

The accurate identification of faults and fractures from 3D seismic data is essential for subsurface interpretation, mapping, and reservoir characterization. The effectiveness of fault identification using the CNN framework strongly depends on the expansiveness of the training dataset and the associated labeling. The synthetic samples can ensure the accuracy of the labels but might not cover all features encountered in the actual seismic data recorded in the field. Pre-training on real seismic images would require labeling a great number of images, which would have been a major undertaking for such a project. Opting for a pre-trained CNN model to predict and interpret seismic faults on the 3D seismic volume and using the UNET topology offered the most pragmatic approach. Faults identified by the pre-trained CNN were expressed better than those of manual interpretation guided by the variance attribute. The three seismic interpretation scenarios that were detailed above demonstrate that, although most of the major faults identified on CNN are seen on the variance cube, some minor faults are seen on one and not on the other. The automated fault identification using the pre-trained CNN on the seismic dataset significantly reduced the interpretation time when compared to that of the manual fault identification and would be the preferred approach in future interpretation projects.

Author Contributions: Conceptualization, I.B.; methodology, M.M.I. and I.B.; software, M.M.I., I.B., M.E. and O.D.A.; validation, I.B., M.E., S.E. and M.M.I.; formal analysis, M.E., S.E., I.B., N.A.S., I.B. and M.M.I.; investigation, M.E.; resources, M.E.; data curation, M.E.; writing—original draft preparation, M.M.I.; writing—review and editing, M.M.I., I.B., M.E., S.E., N.A.S. and O.D.A.; visualization, M.E. and I.B.; supervision, M.E.; project administration, M.E.; funding acquisition, M.E. All authors have read and agreed to the published version of the manuscript.

Funding: This research was supported through the following project: “Machine Learning Application in lithology and fluid properties Prediction utilizing seismic and well log data for optimal reservoir characterization”. The grant cost center: 015LC0-420, grant type: YUTP-FRG 1/2022, awarded to Mohamed Elsaadany.

Institutional Review Board Statement: Not applicable.

Informed Consent Statement: Not applicable.

Data Availability Statement: The associated datasets used in this study are open source from Geoscience Australia. All data are available at <https://nopims.dmp.wa.gov.au/Nopims/> accessed on 20 August 2022.

Acknowledgments: The authors would like to especially thank PETRONAS for funding this project that’s cost center is 01015LC0-420 and the type of grant: YUTP-FRG 1/2022. We thank SLB for giving us a license of the Petrel software (Version 2020) that we used for seismic interpretation and visualization to the Center for Subsurface Seismic Imaging (CSI), University Technology PETRONAS, Malaysia. Our thanks also go to Geophysical Insights for donating the Paradise software that we used for deep learning-based fault prediction. Many thanks go to the anonymous editors and reviewers for providing insightful suggestions on improving the paper’s quality.

Conflicts of Interest: The authors declare no conflict of interest. The funders had no role in the structure of the study; in acquiring, analyzing, or interpreting the data; in the composition of the manuscript; or in the decision to publish the results.

References

1. Basir, H.M.; Javaherian, A.; Yarak, M. T Multi-attribute ant-tracking and neural network for fault detection: A case study of an Iranian oilfield. *J. Geophys. Eng.* **2013**, *10*, 015009. [[CrossRef](#)]
2. Cunha, A.; Pochet, A.; Lopes, H.; Gattass, M. Seismic fault detection in real data using transfer learning from a convolutional neural network pre-trained with synthetic seismic data. *Comput. Geosci.* **2020**, *135*, 104344. [[CrossRef](#)]
3. Di, H.; Wang, Z.; AlRegib, G. *Seismic Fault Detection from Post-Stack Amplitude by Convolutional Neural Networks*; European Association of Geoscientists & Engineers: Utrecht, The Netherlands, 2018; Volume 2018, pp. 1–5.
4. Otchere, D.A.; Tackie-Otoo, B.N.; Mohammad, M.A.A.; Ganat, T.O.A.; Kuvakin, N.; Miftakhov, R.; Efremov, I.; Bazanov, A. Improving seismic fault mapping through data conditioning using a pre-trained deep convolutional neural network: A case study on Groningen field. *J. Pet. Sci. Eng.* **2022**, *213*, 110411. [[CrossRef](#)]
5. Bond, C.E. Uncertainty in structural interpretation: Lessons to be learnt. *J. Struct. Geol.* **2015**, *74*, 185–200. [[CrossRef](#)]
6. Alcalde, J.; Bond, C.E.; Johnson, G.; Ellis, J.F.; Butler, R.W. Impact of seismic image quality on fault interpretation uncertainty. *GSA Today* **2017**, *27*, 2. [[CrossRef](#)]
7. Oumarou, S.; Mabrouk, D.; Tabod, T.C.; Marcel, J.; Ngos, S., III; Essi, J.M.A.; Kamguia, J. Seismic attributes in reservoir characterization: An overview. *Arab. J. Geosci.* **2021**, *14*, 402. [[CrossRef](#)]
8. Mousavi, J.; Radad, M.; Monfared, M.S.; Kahoo, A.R. Fault Enhancement in Seismic Images by Introducing a Novel Strategy Integrating Attributes and Image Analysis Techniques. *Pure Appl. Geophys.* **2022**, *179*, 1645–1660. [[CrossRef](#)]
9. Boe, T.H.; Daber, R. Seismic features and the human eye: RGB blending of azimuthal curvatures for enhancement of fault and fracture interpretation. In *SEG Technical Program Expanded Abstracts 2010*; Society of Exploration: London, UK, 2010; pp. 1535–1539.
10. Yan, Z.; Zhang, Z.; Liu, S. Improving Performance of Seismic Fault Detection by Fine-Tuning the Convolutional Neural Network Pre-Trained with Synthetic Samples. *Energies* **2021**, *14*, 3650. [[CrossRef](#)]
11. Ma, X.; Yao, G.; Zhang, F.; Wu, D. 3-D Seismic Fault Detection Using Recurrent Convolutional Neural Networks with Compound Loss. *IEEE Trans. Geosci. Remote Sens.* **2023**, *61*, 5909815. [[CrossRef](#)]
12. Alyaz, A.M.; Bedle, H.; Aydemir, A. Seismic attribute assisted analysis of the interpretational variations in the time and depth migrated datasets: An example from Taranaki Basin, New Zealand. *Mar. Pet. Geol.* **2023**, *155*, 106301. [[CrossRef](#)]
13. Marfurt, K.J.; Kirlin, R.L.; Farmer, S.L.; Bajorich, M.S. 3-D seismic attributes using a semblance-based coherency algorithm. *Geophysics* **1998**, *63*, 1150–1165. [[CrossRef](#)]
14. Wei, X.-L.; Zhang, C.-X.; Kim, S.-W.; Jing, K.-L.; Wang, Y.-J.; Xu, S.; Xie, Z.-Z. Seismic fault detection using convolutional neural networks with focal loss. *Comput. Geosci.* **2021**, *158*, 104968. [[CrossRef](#)]
15. Yan, B.; Wang, T.; Ji, Y.; Yuan, S. Multidirectional Coherence Attribute for Discontinuity Characterization in Seismic Images. *IEEE Geosci. Remote Sens. Lett.* **2022**, *19*, 8026205. [[CrossRef](#)]
16. Sui, J.; Zheng, X.; Zeng, Q.; Yang, Z.; Gan, L.; Hu, T. Seismic Coherence Attribute Based on Eigenvectors and Its Application. *IEEE Geosci. Remote Sens. Lett.* **2023**, *20*, 7504105. [[CrossRef](#)]
17. Wang, S.; Yuan, S.; Yan, B.; He, Y.; Sun, W. Directional complex-valued coherence attributes for discontinuous edge detection. *J. Appl. Geophys.* **2016**, *129*, 1–7. [[CrossRef](#)]

18. Mora, J.P.; Bedle, H.; Marfurt, K.J. Fault enhancement comparison among coherence enhancement, probabilistic neural networks, and convolutional neural networks in the Taranaki Basin area, New Zealand. In *Interpretation*; Society of Exploration: London, UK, 2022; Volume 10, pp. SE1–SE19. [[CrossRef](#)]
19. Ashraf, U.; Zhang, H.; Anees, A.; Nasir Mangi, H.; Ali, M.; Ullah, Z.; Zhang, X. Application of Unconventional Seismic Attributes and Unsupervised Machine Learning for the Identification of Fault and Fracture Network. *Appl. Sci.* **2020**, *10*, 3864. [[CrossRef](#)]
20. Hale, D. Methods to compute fault images, extract fault surfaces, and estimate fault throws from 3D seismic images. *Geophysics* **2013**, *78*, O33–O43. [[CrossRef](#)]
21. Imran, Q.S.; Siddiqui, N.A.; Latiff, A.H.A.; Bashir, Y.; Khan, M.; Qureshi, K.; Al-Masgari, A.A.-S.; Ahmed, N.; Jamil, M. Automated fault detection and extraction under gas chimneys using hybrid discontinuity attributes. *Appl. Sci.* **2021**, *11*, 7218. [[CrossRef](#)]
22. Kim, M.; Yu, J.; Kang, N.-K.; Kim, B.-Y. Improved Workflow for Fault Detection and Extraction Using Seismic Attributes and Orientation Clustering. *Appl. Sci.* **2021**, *11*, 8734. [[CrossRef](#)]
23. Lyu, F.; Zhou, H.; Liu, J.; Zhou, J.; Tao, B.; Wang, D. A buried hill fault detection method based on 3D U-SegNet and transfer learning. *J. Pet. Sci. Eng.* **2022**, *218*, 110917. [[CrossRef](#)]
24. Di, H.; Gao, D. 3D seismic flexure analysis for subsurface fault detection and fracture characterization. *Pure Appl. Geophys.* **2017**, *174*, 747–761. [[CrossRef](#)]
25. Qi, X.; Marfurt, K. Volumetric aberrancy to map subtle faults and flexures. In Proceedings of the 2017 SEG International Exposition and Annual Meeting, Houston, TX, USA, 24–29 September 2017; pp. 3443–3447.
26. Aqrabi, A.A.; Boe, T.H. Improved fault segmentation using a dip guided and modified 3D Sobel filter. In *SEG Technical Program Expanded Abstracts 2011: Society of Exploration Geophysicists*; Society of Exploration: London, UK, 2011; pp. 999–1003.
27. Qi, J.; Zhang, B.; Lyu, B.; Marfurt, K. Seismic attribute selection for machine-learning-based facies analysis. *Geophysics* **2020**, *85*, O17–O35. [[CrossRef](#)]
28. Li, F.; Lyu, B.; Qi, J.; Verma, S.; Zhang, B. Seismic Coherence for Discontinuity Interpretation. *Surv. Geophys.* **2021**, *42*, 1229–1280. [[CrossRef](#)]
29. Di, H.; Gao, D. Gray-level transformation and Canny edge detection for 3D seismic discontinuity enhancement. *Comput. Geosci.* **2014**, *72*, 192–200. [[CrossRef](#)]
30. Rijks, E.; Jauffred, J. Attribute extraction: An important application in any detailed 3-D interpretation study. *Lead. Edge* **1991**, *10*, 11–19. [[CrossRef](#)]
31. Maduna, N.G.; Manzi, M.S.D.; Bourdeau, J.E.; Jinnah, Z. 3D reflection seismic imaging of natural gas/fluid escape features in the deep[1]p-water Orange Basin of South Africa. *Mar. Geophys. Res.* **2023**, *44*, 17. [[CrossRef](#)]
32. Zhang, B.; Liu, Y.; Pelissier, M.; Hemstra, N. Semiautomated fault interpretation based on seismic attributes. *Interpretation* **2014**, *2*, SA11–SA19. [[CrossRef](#)]
33. Machado, G.; Alali, A.; Hutchinson, B.; Olorunsola, O.; Marfurt, K.J. Display and enhancement of volumetric fault images. *Interpretation* **2016**, *4*, SB51–SB61. [[CrossRef](#)]
34. Di, H.; Shafiq, M.A.; AlRegib, G. Seismic-fault detection based on multiattribute support vector machine analysis. In Proceedings of the 2017 SEG International Exposition and Annual Meeting, Houston, TX, USA, 24–29 September 2017.
35. Di, H.; Shafiq, M.; AlRegib, G. Patch-level MLP classification for improved fault detection. In *SEG Technical Program Expanded Abstracts 2018: Society of Exploration Geophysicists*; Society of Exploration: London, UK, 2018; pp. 2211–2215.
36. Zhao, T.; Jayaram, V.; Roy, A.; Marfurt, K.J. A comparison of classification techniques for seismic facies recognition. In *Interpretation*; Society of Exploration: London, UK, 2015; Volume 3, pp. SAE29–SAE58.
37. Struckmeyer, H.L.; Blevin, J.E.; Sayers, J.; Totterdell, J.M.; Baxter, K.; Cathro, D.L. *Structural Evolution of the Browse Basin, Northwest Shelf: New Concepts from Deep-Seismic Data*; PESA: Beaumaris, Australia, 1998.
38. Patadiya, P.; Parmar, J.; Ramalingam, V.; Singh, A. *Hydrocarbon Source Rock Characterization and Basin Modelling, A Case Study from Poseidon Field, Browse Basin, Australia*; European Association of Geoscientists & Engineers: Utrecht, The Netherlands, 2023; pp. 1–5. [[CrossRef](#)]
39. Dixit, A.; Mandal, A. Detection of gas chimney and its linkage with deep-seated reservoir in poseidon, NW shelf, Australia from 3D seismic data using multi-attribute analysis and artificial neural network approach. *J. Nat. Gas Sci. Eng.* **2020**, *83*, 103586. [[CrossRef](#)]
40. Farfour, M.; El-Ghali, M.A.K.; Gaci, S.; Moustafa, M.S.H.; Siddiqui, N.A. Seismic attributes for hydrocarbon detection and reservoir characterization: A case study from Poseidon field, Northwestern Australia. *Arab. J. Geosci.* **2021**, *14*, 24. [[CrossRef](#)]
41. Hoffman, N.; Hill, K.; Ellis, G.; Baillie, P.; Munson, T. Structural-stratigraphic evolution and hydrocarbon prospectivity of the deep-water Browse Basin, Northwest Shelf, Australia. In Proceedings of the Timor Sea Symposium, Timor Sea Petroleum Geoscience, Darwin, Australia, 19–20 June 2003; pp. 19–20.
42. Farfour, M.; Foster, D. Machine learning and seismic attributes for prospect identification and risking: An example from offshore Australia. In Proceedings of the SEG/AAPG International Meeting for Applied Geoscience & Energy, Houston, TX, USA, 28 August–2 September 2022.
43. Le Poidevin, S.R.; Temple, P.; Edwards, D.S.; Kuske, T. *Australian Petroleum Accumulations Report 7 Browse Basin: Western Australia and Territory of Ashmore and Cartier Islands Adjacent Area*; Geoscience Australia: Canberra, Australia, 2015.
44. Di, H.; Shafiq, A.; Wang, Z.; Alregib, G. Improving seismic fault detection by super-attribute-based classification. In *Interpretation*; Society of Exploration: London, UK, 2019; Volume 7, pp. 1–56. [[CrossRef](#)]

45. Fehmers, G.C.; Höcker, C.F.W. Fast structural interpretation with structure-oriented filtering. *Geophysics* **2003**, *68*, 1286–1293. [[CrossRef](#)]
46. Laudon, C.; Qi, J.; Rondon, A.; Rouis, L.; Kabazi, H. An enhanced fault detection workflow combining machine learning and seismic attributes yields an improved fault model for Caspian Sea asset. *First Break*. **2021**, *39*, 53–60. [[CrossRef](#)]

Disclaimer/Publisher’s Note: The statements, opinions and data contained in all publications are solely those of the individual author(s) and contributor(s) and not of MDPI and/or the editor(s). MDPI and/or the editor(s) disclaim responsibility for any injury to people or property resulting from any ideas, methods, instructions or products referred to in the content.